

# Distilling two-center-interference information during tunneling of aligned molecules with orthogonally polarized two-color laser fields

F. Gao,<sup>1</sup> Y. J. Chen,<sup>1,\*</sup> G. G. Xin,<sup>2,3,†</sup> J. Liu,<sup>4,5</sup> and L. B. Fu<sup>5,6,‡</sup>

<sup>1</sup>*College of Physics and Information Technology, Shaan'xi Normal University, Xi'an 710119, China*

<sup>2</sup>*School of Physics, Northwest University, Xi'an 710127, China*

<sup>3</sup>*Beijing Computational Science Research Center, Beijing 100193, China*

<sup>4</sup>*National Laboratory of Science and Technology on Computational Physics,*

*Institute of Applied Physics and Computational Mathematics, Beijing 100088, China*

<sup>5</sup>*CAPT, HEDPS, and IFSA Collaborative Innovation Center of MoE, Peking University, Beijing 100871, China*

<sup>6</sup>*Graduate School, China Academy of Engineering Physics, Beijing 100193, China*

(Received 20 August 2017; published 19 December 2017)

When electrons tunnel through a barrier formed by the strong laser field and the two-center potential of a diatomic molecule, a double-slit-like interference can occur. However, this interference effect can not be probed directly right now, as it is strongly coupled with other dynamical processes during tunneling. Here, we show numerically and analytically that orthogonally polarized two-color (OTC) laser fields are capable of resolving the interference effect in tunneling, while leaving clear footprints of this effect in photoelectron momentum distributions. Moreover, this effect can be manipulated by changing the relative field strength of OTC fields.

DOI: [10.1103/PhysRevA.96.063414](https://doi.org/10.1103/PhysRevA.96.063414)

## I. INTRODUCTION

Tunneling is one of the most amazing and subtle phenomena in quantum mechanics without classical correspondence. It has been studied continuously since the establishment of quantum mechanics [1–10]. However, the tunneling process, i.e., how a bound electron passes through a classically forbidden potential barrier, is still ambiguous. Very recently, the development of attosecond technology, based on ionization and high-order harmonic generation (HHG) of atoms in strong laser fields, has allowed one to investigate this problem experimentally, while pushing the study on the problem to an unprecedented height [11–14]. Some important and intriguing issues associated with tunneling have been addressed, such as tunneling time [15–18], nonadiabatic effects [19], excited tunneling [20,21], instantaneous momentum at exit [22], and recollisions under the barrier [23].

Besides the tunneling mentioned above, quantum interference is another important phenomenon for microscopic systems. Diatomic molecules with two-center characteristics make them ideal candidates for studying the double-slit-like interference effect on the atomic scale [24]. Recently, two-center interference in the recombination process (the contrary process of strong-field tunneling ionization) of HHG from aligned molecules has been studied in theories and experiments with high time-space resolution [25–31]. One can expect that the interference effect relating to the molecular structure will also play a role in tunneling when the electron passes through the barrier formed by the laser field and the molecular potential. However, this role is not easy to measure and resolve in experiments [32–34], as the structure of the molecule is distorted remarkably by the strong external field in tunneling. Theoretical studies showed that the interference in tunneling

can enhance the whole ionization yields of the molecule in linearly polarized laser fields [35], but this interference-induced enhancement is not self-evident in experiments. The question of how this interference effect in tunneling can be probed unambiguously with an experimentally accessible manner is still open.

Recently, it has been shown that photoelectron momentum spectra of atoms in elliptically polarized fields or orthogonally polarized two-color (OTC) fields [15–19,36–42] include ultrafast electron dynamical information and have wide applications in attosecond measurements. We expect that relevant momentum spectra of molecules can also reveal some interference information in tunneling.

In this paper, we study photoelectron momentum distributions of aligned molecules of  $\text{H}_2^+$  with OTC fields, consisting of a strong fundamental field and a weak second harmonic field, through numerical solution of the time-dependent Schrödinger equation (TDSE). For  $\theta = 0^\circ$  or  $\theta = 90^\circ$  ( $\theta$ , the angle between the molecular axis and the polarization axis of the fundamental field), the calculated momentum distribution is symmetric with respect to  $p_x = 0$  ( $p_x$  is the momentum along the fundamental field). However, for  $\theta = 45^\circ$ , the distribution presents a strong asymmetry for  $p_x = 0$  [see Fig. 1(b)]. We show that this asymmetry arises from the interference of the electronic wave packet between these two atomic cores of the molecule in the tunneling process. When the strong fundamental field plays a dominant role in ionization, the weak second-harmonic field serves as a “hand” to modulate the direction of the tunneling electron momentum in the two-dimensional polarization space; therefore the interference pattern is changed. This modulation depends on the molecular alignment, resulting in an orientation-dependent asymmetry of the momentum distribution.

## II. NUMERICAL METHOD

We assume that the fundamental field is along the  $x$  axis, the additional second-harmonic field is along the  $y$  axis, and

\*chenyjhb@gmail.com

†xinguo@nwu.edu.cn

‡lbfu@iapcm.ac.cn

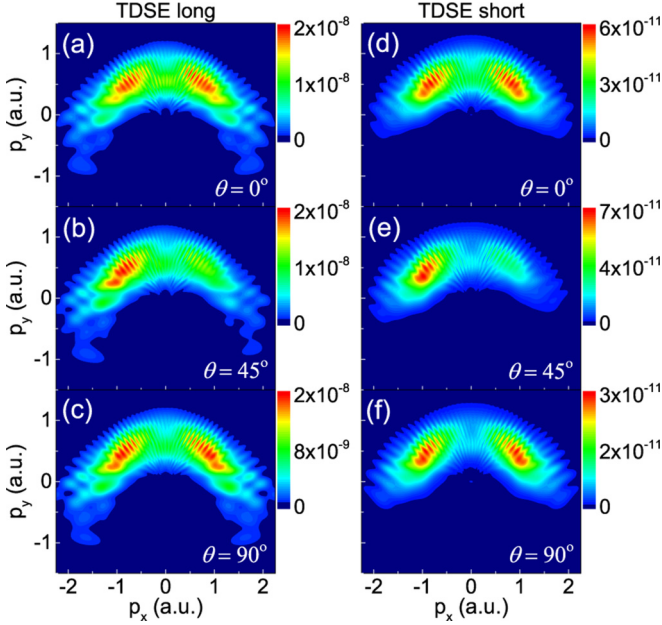


FIG. 1. Photoelectron momentum distributions of  $\text{H}_2^+$  with TDSE simulations of long-range potential (left column) and short-range potential (right) at different angles  $\theta$ . The laser parameters used are  $I = 5 \times 10^{14}$  W/cm $^2$  and  $\lambda = 800$  nm for the fundamental field, and  $I = 1.25 \times 10^{14}$  W/cm $^2$  and  $\lambda = 400$  nm for the second-harmonic field.

the molecular axis is located in the  $xy$  plane. The Hamiltonian of the molecular system studied here has the following form:  $H(t) = \mathbf{p}^2/2 + V(\mathbf{r}) + \mathbf{r} \cdot \mathbf{E}(t)$  (in atomic units of  $\hbar = e = m_e = 1$ ). Here,  $V(\mathbf{r})$  is the Coulomb potential, which has the form of  $V(\mathbf{r}) = -Ze^{-\rho r_1}/\sqrt{r_1^2 + \xi} - Ze^{-\rho r_2}/\sqrt{r_2^2 + \xi}$ , with  $r_{1,2}^2 = (x \pm \frac{R}{2} \cos \theta)^2 + (y \pm \frac{R}{2} \sin \theta)^2$ .  $\rho$  is the screening parameter, with  $\rho = 0$  for the long-range potential and  $\rho = 0.5$  for the short-range one.  $R = 2$  a.u. is the internuclear distance,  $\xi = 0.1$  is the smoothing parameter, and  $Z$  is the effective charge which is adjusted in such a manner that the ionization potential of the model system reproduced here is  $I_p = 1.1$  a.u.

The term  $\mathbf{E}(t)$  is the electric field of OTC fields, which has the form of  $\mathbf{E}(t) = \hat{\mathbf{e}}_x E_x(t) + \hat{\mathbf{e}}_y E_y(t)$ , with  $E_x(t) = f(t)E_0 \sin(\omega_0 t)$  and  $E_y(t) = \mathcal{E} f(t)E_0 \sin(2\omega_0 t + \phi)$ .  $\hat{\mathbf{e}}_x$  ( $\hat{\mathbf{e}}_y$ ) is the unit vector along the  $x$  ( $y$ ) axis.  $\phi$  is the relative phase between these two colors.  $E_0$  is the maximal laser amplitude relating to the peak intensity  $I$  of the fundamental field  $E_x(t)$ .  $\mathcal{E}$  is the ratio of the maximal laser amplitude for the second-harmonic field  $E_y(t)$  to  $E_0$ .  $\omega_0$  is the laser frequency of  $E_x(t)$  and  $f(t)$  is the envelope function. We use a  $\text{sin}^2$ -shaped laser pulse with a total duration of 30 optical cycles. The TDSE of  $i\dot{\Psi}(t) = H(t)\Psi(t)$  is solved numerically using the spectral method [43]. We work with a grid of  $L_x \times L_y = 410 \times 410$  a.u. The space steps used are  $\Delta x = \Delta y = 0.4$  a.u., and the time step is  $\Delta t = 0.05$  a.u. Unless mentioned elsewhere, the laser parameters used are  $I = 5 \times 10^{14}$  W/cm $^2$ ,  $\omega_0 = 0.057$  a.u. (corresponding to the wavelength of  $\lambda = 800$  nm),  $\phi = 0$ , and  $\mathcal{E} = 0.5$ .

In order to avoid the reflection of the electron wave packet from the boundary and obtain the momentum-space wave function, the coordinate space is split into the inner and the

outer regions, with  $\Psi(t) = \Psi_{\text{in}}(t) + \Psi_{\text{out}}(t)$ , by multiplication using the mask function  $F(\mathbf{r}) = F_1(x)F_2(y)$ . Here,  $F_1(x) = \cos^{1/2}[\pi(|x| - r_x)/(L_x - 2r_x)]$  for  $|x| \geq r_x$  and  $F_1(x) = 1$  for  $|x| < r_x$ .  $r_x = 150$  a.u. is the absorbing boundary at which the Coulomb potential is negligible in comparison with the typical electron quiver energy [ $U_p = E_0^2/(4\omega_0^2)$ ] in the outer region. The form of  $F_2(y)$  is similar to  $F_1(x)$ . In the inner region, the wave function  $\Psi_{\text{in}}(t)$  is propagated with the complete Hamiltonian  $H(t)$ . In the outer region, the time evolution of the wave function  $\Psi_{\text{out}}(t)$  is carried out in momentum space with the Hamiltonian of the free electron in the laser field [44–46]. The mask function is applied at each time interval of 1 a.u. and the obtained new fractions of the outer wave function are added to the momentum-space wave function  $\tilde{\Psi}_{\text{out}}(t)$  from which we obtain the momentum distribution of the photoelectron.

### III. MOMENTUM DISTRIBUTIONS

The calculated photoelectron momentum distributions for  $\text{H}_2^+$  at three typical angles of  $\theta = 0^\circ$ ,  $45^\circ$ , and  $90^\circ$  are presented in the left column of Fig. 1. First, the distributions at different angles show a handlebar-mustache-like structure, which basically agrees with the prediction of the semiclassical two-step model [47] in the diagram of  $p_x(t) = -A_x(t)$  versus  $p_y(t) = -A_y(t)$  (not shown here). Here,  $\mathbf{A}(t) = \hat{\mathbf{e}}_x A_x(t) + \hat{\mathbf{e}}_y A_y(t)$  is the vector potential of  $\mathbf{E}(t)$ .

A remarkable difference between the distributions is that the results at  $\theta = 45^\circ$  [Fig. 1(b)] show a strong asymmetry with respect to the axis of  $p_x = 0$ , while the results at  $\theta = 0^\circ$  [Fig. 1(a)] and  $\theta = 90^\circ$  [Fig. 1(c)] are symmetric. This remarkable asymmetry at  $\theta = 45^\circ$  holds for the short-range potential model (shown in the right column of Fig. 1) where the Coulomb potential decreases rapidly to zero with the increase of the distance from the parent ions. We therefore deduce that the long-range Coulomb effect plays a small role in this asymmetry, and this asymmetry is induced predominantly by the tunneling step. We mention that results at other intermediate angles such as  $\theta = 30^\circ$  and  $50^\circ$  also show the asymmetry, although somewhat weaker than that at  $\theta = 45^\circ$  observed here.

To verify our results, we further perform simulations with strong-field approximations (SFA) [48–51] without the Coulomb effect, and with a semiclassical electron-ensemble model (SEEM) [52,53] without quantum interference. As shown in Fig. 2, the SFA (left column) reproduces the angle-dependent asymmetry and the fine structure of the distributions (the clear interference patterns), while the results of SEEM (right column) are similar and keep symmetry for different orientation angles. The results suggest that this asymmetry arises from quantum effects depending on the molecular orientation.

We mention that the amplitudes of the distributions in Figs. 1 and 2 are not directly comparable with each other as they are obtained with different treatments. Alternatively, in the TDSE simulations, one can decrease the value of the absorbing boundary  $r_{x(y)}$  or use an exponential-type mask function which decreases fast. These treatments will increase the fragment of the outer wave function and improve the comparison between amplitudes of SFA and short-range TDSE, as the main structural characteristics of the TDSE

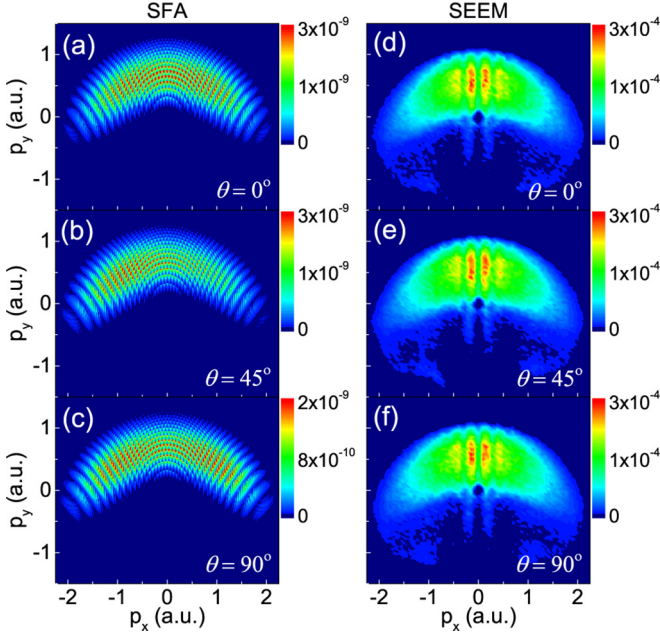


FIG. 2. Same as Fig. 1, except for SFA simulations (left column) and SEEM simulations (right column). The SEEM results have been normalized to the maximum value in each panel.

distributions do not change basically, similar to the simulations in Ref. [45]. In addition, in Fig. 1 in the electron momentum spectrum, there is a gap at  $p_x = 0$  between the two lobes. In the SFA results in Fig. 2, this gap is not remarkable. There are two possible reasons for this gap. First, this gap can be associated with the so-called “frustrated tunneling ionization” arising from the Coulomb effect [54]. Specifically, as the electron tunnels through the barrier with low drift energy, it can be captured by the Coulomb field of the ion. By comparison, the Coulomb effect is absent in the SFA [48]. Second, in our TDSE simulations with splitting the coordinate space into the inner and the outer regions and with the large absorbing boundary, electrons with smaller energies cannot be fully collected in the outer region [44]. When the gap is also there in short-range TDSE simulations which should be similar to SFA calculations, where it is almost absent, we expect that the second reason plays a dominant role. Really, in our extended simulations with decreasing the absorbing boundary, this gap becomes weaker.

#### IV. INTERFERENCE IN TUNNELING

Based on the above comparisons and analyses, in the following, we study the origin of this asymmetry with SFA and focus on the tunneling process. In the SFA, the amplitude of the photoelectron with the drift momentum  $\mathbf{p}$  can be written as  $c(\mathbf{p}) = -i \int_0^{T_p} dt' \mathbf{E}(t') \cdot \mathbf{d}_m[\mathbf{p} + \mathbf{A}(t')] e^{iS(\mathbf{p}, t')}$  [51]. Here  $S(\mathbf{p}, t') = \int_0^{t'} \{[\mathbf{p} + \mathbf{A}(t'')]^2/2 + I_p\} dt''$  is the quasiclassical action and  $T_p$  is the length of the total pulse. The term  $\mathbf{d}_m[\mathbf{p} + \mathbf{A}(t')] = \langle \mathbf{p} + \mathbf{A}(t') | \mathbf{r} | 0 \rangle$  denotes the dipole matrix element for the bound-free transition. With expressing the  $1\sigma_g$  wave function of  $\text{H}_2^+$  in the linear combination of atomic-orbitals-molecular-orbitals (LCAO-MO) approximations [55], we have  $\langle \mathbf{r} | 0 \rangle \sim e^{-\kappa r_a} + e^{-\kappa r_b}$ , with  $\kappa = \sqrt{2I_p}$ ,  $\mathbf{r}_a = \mathbf{r} + \mathbf{R}/2$ , and

$\mathbf{r}_b = \mathbf{r} - \mathbf{R}/2$ . Then the dipole matrix element of the molecule can be written as [35]  $\mathbf{d}_m \approx \cos\{[\mathbf{p} + \mathbf{A}(t')] \cdot \mathbf{R}/2\} \cdot \mathbf{d}_a$ . Here,  $\mathbf{d}_a \sim \langle \mathbf{p} + \mathbf{A}(t') | \mathbf{r} | e^{-\kappa r} \rangle$  is the dipole matrix element of the atom and  $\mathbf{R}$  is the vector between these two atomic centers. In the above expression of  $\mathbf{d}_m$ , only the interference term  $\cos$ , which describes the interference of the electron wave between these two atomic centers of the molecule, is dependent on the molecular alignment. We therefore anticipate that the interference effect characterized by the  $\cos$  term plays an important role in this asymmetric distribution at  $\theta = 45^\circ$ .

Next, we analyze the properties of the interference term  $\cos$  in tunneling. According to the saddle-point equation [49,56,57] of  $[\mathbf{p} + \mathbf{A}(t')]^2/2 + I_p = 0$ , which formulates the strong-field tunneling process, and considering the OTC field, we have  $[\mathbf{p} + \mathbf{A}(t')]^2/2 = \{\tilde{\mathbf{e}}_x[p_x + A_x(t')] + \tilde{\mathbf{e}}_y[p_y + A_y(t')]\}^2/2 = -I_p$ . The solution of the saddle-point equation requires a complex time  $t'$  with  $t' = t_R + it_I$ . Accordingly, the components of the vector potential  $\mathbf{A}(t')$  are also complex with  $A_{x(y)}(t') = A_{R,x(y)}(t') + iA_{I,x(y)}(t')$ . With assuming that the real parts of  $A_{x(y)}(t')$  agree with the relations  $p_x + A_{R,x}(t') = 0$  and  $p_y + A_{R,y}(t') = 0$ , we have  $[\tilde{\mathbf{e}}_x A_{I,x}(t') + \tilde{\mathbf{e}}_y A_{I,y}(t')]^2/2 = \mathbf{A}_I^2(t')/2 = I_p$ . Then one obtains  $A_I(t') = \sqrt{2I_p} = \kappa$ , and the interference term  $\cos\{[\mathbf{p} + \mathbf{A}(t')] \cdot \mathbf{R}/2\}$  has the following form:

$$\cos\left(\frac{i\kappa R \cos\theta_I}{2}\right) = \left(e^{\frac{\kappa R \cos\theta_I}{2}} + e^{-\frac{\kappa R \cos\theta_I}{2}}\right)/2. \quad (1)$$

Here,  $\theta_I$  is the angle between the vector  $\mathbf{A}_I(t') = \tilde{\mathbf{e}}_x A_{I,x}(t') + \tilde{\mathbf{e}}_y A_{I,y}(t')$  and the molecular axis.

It should be noted that according to the above analyses, the real parts  $[A_{R,x}(t')$  and  $A_{R,y}(t')]$  of the vector potential at the moment of tunneling, given by the saddle-point equation, are related to the values of the final momenta (i.e.,  $p_x$  and  $p_y$ ), while the imaginary parts  $[A_{I,x}(t')$  and  $A_{I,y}(t')]$  influence the amplitudes of the final momenta. In the following, we discuss how this influence occurs and its relationship with the orientation angle  $\theta$ .

We calculate the complex saddle-point time  $t'$  approximately, following the discussions just above Eq. (1). The real part  $t_R$  of the complex time  $t'$  is usually considered as the ionization time  $t$  of the system. Once the complex time  $t'$  is obtained, we can evaluate the different components of the vector potential  $\mathbf{A}(t')$ . In Fig. 3(a), we plot the imaginary components  $A_{I,x}(t')$  (bold blue-solid line) and  $A_{I,y}(t')$  (bold red-dashed line) with the laser parameters as in Fig. 1. We focus on two typical ionization times,  $t_1 = \frac{T}{4} - \delta$  and  $t_2 = \frac{T}{4} + \delta$  (relating to the complex saddle-point times  $t'_1$  and  $t'_2$ , respectively), with a small quantity  $\delta$  in half a laser cycle of the fundamental field. These two times around the peak time  $\frac{T}{4}$  of  $E_x(t)$  are expected to contribute importantly to ionization. Accordingly, a sketch of the components  $A_{I,x}$  and  $A_{I,y}$  and the combined vector  $\mathbf{A}_I$  at different angles  $\theta$  around these two times is presented in Fig. 3(b). Note, at the time  $t_1$ ,  $A_{I,x}(t'_1) < 0$  and  $A_{I,y}(t'_1) < 0$ , and at  $t_2$ ,  $A_{I,x}(t'_2) < 0$  and  $A_{I,y}(t'_2) > 0$ . For both cases of  $\theta = 0^\circ$  and  $\theta = 90^\circ$ , we have  $|\cos[\theta_I(t_1)]| = |\cos[\theta_I(t_2)]|$ , where  $\theta_I(t)$  denotes the value of the angle  $\theta_I$  at the time  $t$ . Then we also have  $|\cos(\frac{i\kappa R \cos\theta_I(t_1)}{2})| = |\cos(\frac{i\kappa R \cos\theta_I(t_2)}{2})|$ , implying that the interference term gives the same contribution to the direct

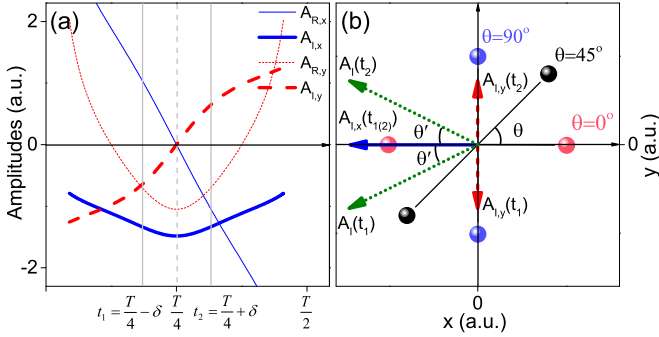


FIG. 3. (a) A sketch of the imaginary components  $A_{I,x}(t')$  (bold blue-solid) and  $A_{I,y}(t')$  (bold red-dashed) of the complex vector potential  $\mathbf{A}(t')$  as functions of the ionization time  $t$  (i.e., the real part  $t_R$  of the complex saddle-point time  $t' = t_R + it_I$ ). The real components  $A_{R,x(y)}(t')$  are also plotted with thin curves here. (b) The combined vector  $\mathbf{A}_I(t)$  (olive-dotted arrows) of the components  $A_{I,x}(t)$  (blue-solid arrows) and  $A_{I,y}(t)$  (red-dashed arrows) at  $\theta = 0^\circ$  (magenta spheres),  $45^\circ$  (black spheres), and  $90^\circ$  (blue spheres). We focus on two typical ionization times of  $t_1 = \frac{T}{4} - \delta$  and  $t_2 = \frac{T}{4} + \delta$  [gray-solid lines in panel (a)] in half a laser cycle of the fundamental field  $E_x(t)$  around the peak time  $t = \frac{T}{4}$  (gray-dashed line).  $T$  is the laser cycle.  $\theta'$  is the angle between  $\mathbf{A}_I(t)$  and the  $x$  axis.

electron (born at  $t_1 = \frac{T}{4} - \delta$ ) and the rescattering electron (born at  $t_2 = \frac{T}{4} + \delta$ ) here. This situation is different for  $\theta = 45^\circ$ , at which  $|\cos[\theta_I(t_1)]| = |\cos(\theta - \theta')|$  and  $|\cos[\theta_I(t_2)]| = |\cos(\theta + \theta')|$ . Here,  $\theta'$  denotes the angle between the vector  $\mathbf{A}_I$  and the  $x$  axis, as indicated in Fig. 3(b). Because the amplitude of  $E_y(t)$  is smaller than that of  $E_x(t)$ , one can expect that the angle  $\theta'$  defined here is smaller than  $45^\circ$ . We therefore have  $|\cos(\theta + \theta')| < \cos 45^\circ < |\cos(\theta - \theta')|$ . Then we arrive at  $|\cos(\frac{i\kappa R \cos \theta_I(t_1)}{2})| > |\cos(\frac{i\kappa R \cos \theta_I(t_2)}{2})|$ , which implies that due to the interference effect, the electron born at  $t_1 = \frac{T}{4} - \delta$  with momentum  $p_x(t_1) = -A_{R,x}(t'_1) < 0$  has a larger amplitude than that born at  $t_2 = \frac{T}{4} + \delta$  with  $p_x(t_2) = -A_{R,x}(t'_2) > 0$ . Similar analyses also go for the times of  $\frac{3T}{4} - \delta$  and  $\frac{3T}{4} + \delta$ . These analyses explain why the distributions at  $\theta = 45^\circ$  in Figs. 1(b) and 2(b) have amplitudes for  $p_x < 0$  larger than those for  $p_x > 0$ . In addition, for  $\theta = 135^\circ$ , our analyses also predict larger amplitudes for  $p_x > 0$  in comparison with those for  $p_x < 0$ , which is also in agreement with our extended simulations.

Note, for linearly polarized one-color laser fields, we have  $\theta_I = \theta$ . In this situation, the term  $\cos(\frac{i\kappa R \cos \theta}{2})$  contributes equally to the amplitude  $c(\mathbf{p})$  for different momenta  $\mathbf{p}$  [35]. As a result, the asymmetric momentum distribution at  $\theta = 45^\circ$ , which characterizes the interference effect in tunneling, disappears (also see Fig. 4). In addition, similar to the linear polarization case, in OTC fields, there also exist two saddle points per cycle contributing comparably to the same momentum. The interference of these two saddle points (intracycle interference) induces the remarkable streaks (the clear interference patterns) in the momentum distributions in the quantum results in Figs. 1 and 2.

In our above analyses based on the SFA and associated with internuclear interference effects, the influence of the

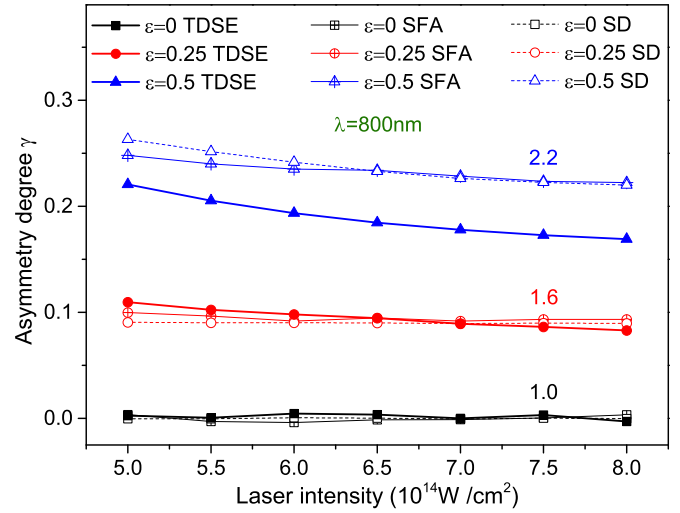


FIG. 4. Asymmetry degree  $\gamma$  of the photoelectron momentum distribution of  $\text{H}_2^+$  at  $\theta = 45^\circ$  for different laser parameters, obtained with TDSE, SFA, and saddle-point (SD) simulations. For comparison, results in each SD curve have been divided by a constant, as indicated by the colored numbers.

molecular structure on ionization is not fully considered and the contributions of excited states to ionization are also omitted. These factors can play an important role in the orientation dependence of ionization for molecules with more complex symmetries such as  $\text{CO}_2$  [58] and larger internuclear distances such as stretched molecular ions [59–61]. More generally, the asymmetric momentum distribution observed in Fig. 1 can also be understood with the orientation-dependent ionization. (i) In the first and fourth quarters of the fundamental period with  $0 < t < T = 2\pi/\omega_0$ , we have the following: (a) electrons released during this time contribute to the photoelectron momentum distribution at  $p_x < 0$ , (b) the  $x$  and  $y$  components of the field have the same sign, and hence (c) the angle between the instantaneous field and the molecular axis for the case  $\theta = 45^\circ$  is less than  $45^\circ$ . (ii) In the second and third quarters of the fundamental period with  $0 < t < T = 2\pi/\omega_0$ , we have the following: (a) electrons released during this time contribute to the photoelectron momentum distribution at  $p_x > 0$ , (b) the  $x$  and  $y$  components of the field have opposite signs, and hence (c) the angle between the instantaneous field and the molecular axis for the case  $\theta = 45^\circ$  is larger than  $45^\circ$ . (iii) The tunneling ionization rate of  $\text{H}_2^+$  is known to monotonically decrease as the angle between the ionizing field and the internuclear axis grows from  $\theta = 0^\circ$  to  $90^\circ$ . The combination of these facts also explains the asymmetry seen in the TDSE results in Fig. 1. From this point of view, our above interference-related discussions can also give suggestions on the complex orientation dependence of ionization rates of molecules in strong OTC fields.

## V. ASYMMETRY DEGREE

To further describe the orientation-related asymmetry, we define the parameter  $\gamma$  as  $\gamma = (A_{p_x^-} - A_{p_x^+}) / (A_{p_x^-} + A_{p_x^+})$  to describe the asymmetric degree of the photoelectron momentum distribution. Here,  $A_{p_x^\pm}$  is the integral of the

amplitude  $|c(\mathbf{p})|^2$  over the electron momentum  $\mathbf{p}$  with  $p_x < 0$  and  $A_{p_x^+}$  is that for  $p_x > 0$ . The values of the parameter  $\gamma$  evaluated with TDSE and SFA simulations are presented in Fig. 4. One can observe from Fig. 4 that the TDSE predictions (solid symbols) increase with the increase of  $\mathcal{E}$ , in agreement with the SFA results (hollow-plus symbols). However, as the laser intensity of the fundamental field increases, the TDSE results at  $\mathcal{E} > 0$  decrease on the whole. This phenomenon is also reproduced by the SFA.

All of the above results can be understood by performing saddle-point analyses, as introduced before. Relevant saddle-point results are also presented in Fig. 4, where the amplitude  $c(\mathbf{p})$  is calculated with  $c(\mathbf{p}) \approx -i \sum_s (2\pi / \det A_2)^{1/2} \mathbf{E}(t'_s) \cdot \mathbf{d}_m[\mathbf{p} + \mathbf{A}(t'_s)] e^{iS(\mathbf{p}, t'_s)}$  [51]. Here, the sum is over the saddle points  $t'_s$  and the determinant  $A_2$  is the second-order derivative of  $iS$  with  $S \equiv S(\mathbf{p}, t'_s)$ . In the above expression of  $c(\mathbf{p})$ , the dipole term  $\mathbf{d}_m[\mathbf{p} + \mathbf{A}(t'_s)]$  is singular at  $t'_s$ . By carrying out the transformation  $\mathbf{r} \cdot \mathbf{E}(t) \rightarrow V(\mathbf{r})$  in the preexponential factor of the expression, one can get rid of the singularity as in the atomic case [62]. This treatment is particularly useful for a short-range or zero-range potential since these restrict the range of the spatial integration in the dipole matrix element [50]. Alternatively, for the Coulomb potential, this singularity can also be overcome with using the modified saddle-point method [51]. Here, we treat this singularity following the latter.

This asymmetry degree evaluated roughly with the saddle-point method is larger than the SFA one at  $\mathcal{E} > 0$ . The reason could be that the saddle-point equation in the OTC fields is solved here with the assumptions discussed above Eq. (1), and some relevant saddle points may not be included in our simulations. However, the trends of the scaled saddle-point curves (hollow symbols) agree with the SFA ones (hollow-plus symbols) in Fig. 4. We therefore expect that the saddle-point analysis gives an applicable description of the origin of this asymmetry here. The results in Fig. 4 also give suggestions on the choice of laser parameters for observing this asymmetry

in experiments. We stress that with a more accurate saddle-point approximation, the derived asymmetries in Fig. 4 can be identical via the numerical and the saddle-point SFA for the given parameters and there would be no need for scaling.

Finally, we have also extended our simulations to three-dimensional  $\text{H}_2^+$  and to model  $\text{N}_2$  with  $3\sigma$  symmetry (for which a model potential is used, as introduced in Refs. [21,63,64]). The changes of the relative phase  $\phi$  (up to  $\phi = 30^\circ$ ) and the laser wavelength (from  $\lambda = 600$  to  $1000$  nm), as well as the further increase of  $\mathcal{E}$  (up to  $\mathcal{E} = 1$ ), in relevant calculations have also been executed. In all cases, this remarkable angle-dependent asymmetry can still be observed in our simulations.

## VI. CONCLUSIONS

In summary, we have studied photoelectron momentum distributions from aligned diatomic molecules in OTC fields. A strong asymmetry is observed in the distribution for  $\theta = 45^\circ$ , which is identified as arising from the interference of the tunneling electron as it passes through the laser-molecule barrier. This interference is modulated by the second-harmonic field and this modulation depends on the molecular orientation, leading to an orientation-dependent asymmetry of the momentum distribution. This effect associated with OTC fields is expected to be general for molecules with multicenter characteristics. It can be used as a tool to distill the structural information of the molecule from the electronic continuum wave packet and to probe the dynamics of the tunneling electron as it escapes from aligned molecules.

## ACKNOWLEDGMENTS

This work is supported by the National Basic Research Program of China (973 Program) (Grant No. 2013CB834100) and the National Natural Science Foundation of China (Grants No. 91750111, No. 11404259, No. 11475027, No. 11575027, and No. 11725417).

- 
- [1] L. A. MacColl, *Phys. Rev.* **40**, 621 (1932).  
 [2] L. V. Keldysh, *Sov. Phys. JETP* **20**, 1307 (1965).  
 [3] M. V. Ammosov, N. B. Delone, and V. P. Krainov, *Sov. Phys. JETP* **64**, 1191 (1986).  
 [4] E. H. Hauge and J. A. Støvneng, *Rev. Mod. Phys.* **61**, 917 (1989).  
 [5] R. Landauer and T. Martin, *Rev. Mod. Phys.* **66**, 217 (1994).  
 [6] X. M. Tong, Z. X. Zhao, and C. D. Lin, *Phys. Rev. A* **66**, 033402 (2002).  
 [7] M. Razhavy, *Quantum Theory of Tunneling* (World Scientific, Singapore, 2003).  
 [8] H. G. Winful, *Phys. Rep.* **436**, 1 (2006).  
 [9] K. Maji, C. K. Mondal, and S. P. Bhattacharyya, *Int. Rev. Phys. Chem.* **26**, 647 (2007).  
 [10] L. Torlina, F. Morales, J. Kaushal, I. Ivanov, A. Kheifets, A. Zielinski, A. Scrinzi, H. G. Muller, S. Sukiasyan, M. Ivanov, and O. Smirnova, *Nat. Phys.* **11**, 503 (2015).  
 [11] P. B. Corkum and F. Krausz, *Nat. Phys.* **3**, 381 (2007).  
 [12] D. Shafir, H. Soifer, B. D. Bruner, M. Dagan, Y. Mairesse, S. Patchkovskii, M. Yu. Ivanov, O. Smirnova, and N. Dudovich, *Nature (London)* **485**, 343 (2012).  
 [13] L. Gallmann, C. Cirelli, and U. Keller, *Annu. Rev. Chem.* **63**, 447 (2012).  
 [14] F. Lépine, M. Y. Ivanov, and M. J. J. Vrakking, *Nat. Photon.* **8**, 195 (2014).  
 [15] P. Eckle, A. N. Pfeiffer, C. Cirelli, A. Staudte, R. Dörner, H. G. Muller, M. Büttiker, and U. Keller, *Science* **322**, 1525 (2008).  
 [16] P. Eckle, M. Smolarski, P. Schlup, J. Biegert, A. Staudte, M. Schöffler, H. G. Muller, R. Dörner, and U. Keller, *Nat. Phys.* **4**, 565 (2008).  
 [17] A. N. Pfeiffer, C. Cirelli, M. Smolarski, D. Dimitrovski, M. Abu-samha, L. B. Madsen, and U. Keller, *Nat. Phys.* **8**, 76 (2012).  
 [18] N. Camus, E. Yakaboylu, L. Fechner, M. Klaiber, M. Laux, Y. Mi, K. Z. Hatsagortsyan, T. Pfeifer, C. H. Keitel, and R. Moshhammer, *Phys. Rev. Lett.* **119**, 023201 (2017).  
 [19] M. Klaiber, K. Z. Hatsagortsyan, and C. H. Keitel, *Phys. Rev. Lett.* **114**, 083001 (2015).  
 [20] E. E. Serebryannikov and A. M. Zheltikov, *Phys. Rev. Lett.* **116**, 123901 (2016).  
 [21] S. Wang, J. Cai, and Y. Chen, *Phys. Rev. A* **96**, 043413 (2017).

- [22] N. Teeny, E. Yakaboylu, H. Bauke, and C. H. Keitel, *Phys. Rev. Lett.* **116**, 063003 (2016).
- [23] Th. Keil, S. V. Popruzhenko, and D. Bauer, *Phys. Rev. Lett.* **117**, 243003 (2016).
- [24] M. Lein, N. Hay, R. Velotta, J. P. Marangos, and P. L. Knight, *Phys. Rev. Lett.* **88**, 183903 (2002).
- [25] T. Kanai, S. Minemoto, and H. Sakai, *Nature (London)* **435**, 470 (2005).
- [26] C. Vozzi, F. Calegari, E. Benedetti, J.-P. Caumes, G. Sansone, S. Stagira, M. Nisoli, R. Torres, E. Heesel, N. Kajumba, J. P. Marangos, C. Altucci, and R. Velotta, *Phys. Rev. Lett.* **95**, 153902 (2005).
- [27] Y. J. Chen, J. Liu, and B. Hu, *Phys. Rev. A* **79**, 033405 (2009).
- [28] Y. J. Chen, J. Liu, and B. Hu, *J. Chem. Phys.* **130**, 044311 (2009).
- [29] O. Smirnova, Y. Mairesse, S. Patchkovskii, N. Dudovich, D. Villeneuve, P. Corkum, and M. Yu. Ivanov, *Nature (London)* **460**, 972 (2009).
- [30] H. J. Wörner, J. B. Bertrand, D. V. Kartashov, P. B. Corkum, and D. M. Villeneuve, *Nature (London)* **466**, 604 (2010).
- [31] S. Wang and Y. Chen, *Phys. Rev. A* **92**, 023418 (2015).
- [32] J. Itatani, J. Levesque, D. Zeidler, H. Niikura, H. Pepin, J. C. Kieffer, P. B. Corkum, and D. M. Villeneuve, *Nature (London)* **432**, 867 (2004).
- [33] M. Meckel, A. Staudte, S. Patchkovskii, D. M. Villeneuve, P. B. Corkum, R. Dörner, and M. Spanner, *Nat. Phys.* **10**, 594 (2014).
- [34] M.-M. Liu, M. Li, C. Wu, Q. Gong, A. Staudte, and Y. Liu, *Phys. Rev. Lett.* **116**, 163004 (2016).
- [35] Y. J. Chen and B. Hu, *Phys. Rev. A* **81**, 013411 (2010).
- [36] A. N. Pfeiffer, C. Cirelli, A. S. Landsman, M. Smolarski, D. Dimitrovski, L. B. Madsen, and U. Keller, *Phys. Rev. Lett.* **109**, 083002 (2012).
- [37] L. Zhang, X. Xie, S. Roither, D. Kartashov, Y. L. Wang, C. L. Wang, M. Schoffler, D. Shafir, P. B. Corkum, A. Baltuska, I. Ivanov, A. Kheifets, X. J. Liu, A. Staudte, and M. Kitzler, *Phys. Rev. A* **90**, 061401(R) (2014).
- [38] M. Richter, M. Kunitski, M. Schöffler, T. Jahnke, L. P. H. Schmidt, M. Li, Y. Liu, and R. Dörner, *Phys. Rev. Lett.* **114**, 143001 (2015).
- [39] X. Xie, *Phys. Rev. Lett.* **114**, 173003 (2015).
- [40] J.-W. Geng, W.-H. Xiong, X.-R. Xiao, L.-Y. Peng, and Q. Gong, *Phys. Rev. Lett.* **115**, 193001 (2015).
- [41] M. Richter, M. Kunitski, M. Schoffler, T. Jahnke, L. P. H. Schmidt, and R. Dörner, *Phys. Rev. A* **94**, 033416 (2016).
- [42] S. G. Yu, Y. L. Wang, X. Y. Lai, Y. Y. Huang, W. Quan, and X. J. Liu, *Phys. Rev. A* **94**, 033418 (2016).
- [43] M. D. Feit, J. A. Fleck, Jr., and A. Steiger, *J. Comput. Phys.* **47**, 412 (1982).
- [44] M. Lein, J. P. Marangos, and P. L. Knight, *Phys. Rev. A* **66**, 051404(R) (2002).
- [45] X. M. Tong, K. Hino, and N. Toshima, *Phys. Rev. A* **74**, 031405(R) (2006).
- [46] J. Henkel, M. Lein, and V. Engel, *Phys. Rev. A* **83**, 051401(R) (2011).
- [47] P. B. Corkum, *Phys. Rev. Lett.* **71**, 1994 (1993).
- [48] M. Lewenstein, Ph. Balcou, M. Yu. Ivanov, A. L'Huillier, and P. B. Corkum, *Phys. Rev. A* **49**, 2117 (1994).
- [49] M. Lewenstein, K. C. Kulander, K. J. Schafer, and P. H. Bucksbaum, *Phys. Rev. A* **51**, 1495 (1995).
- [50] W. Becker, F. Grasbon, R. Kopold, D. B. Milošević, G. G. Paulus, and H. Walther, *Adv. At. Mol. Opt. Phys.* **48**, 35 (2002).
- [51] D. B. Milošević, G. G. Paulus, D. Bauer, and W. Becker, *J. Phys. B* **39**, R203 (2006).
- [52] L. B. Fu, J. Liu, J. Chen, and S. G. Chen, *Phys. Rev. A* **63**, 043416 (2001).
- [53] L. B. Fu, G. G. Xin, D. F. Ye, and J. Liu, *Phys. Rev. Lett.* **108**, 103601 (2012).
- [54] T. Nubbemeyer, K. Gorling, A. Saenz, U. Eichmann, and W. Sandner, *Phys. Rev. Lett.* **101**, 233001 (2008).
- [55] Y. J. Chen and B. Hu, *Phys. Rev. A* **80**, 033408 (2009).
- [56] D. Bauer, D. B. Milošević, and W. Becker, *Phys. Rev. A* **72**, 023415 (2005).
- [57] Y. J. Chen and B. Hu, *J. Chem. Phys.* **131**, 244109 (2009).
- [58] D. Pavičić, K. F. Lee, D. M. Rayner, P. B. Corkum, and D. M. Villeneuve, *Phys. Rev. Lett.* **98**, 243001 (2007).
- [59] T. Seideman, M. Yu. Ivanov, and P. B. Corkum, *Phys. Rev. Lett.* **75**, 2819 (1995).
- [60] T. Zuo and A. D. Bandrauk, *Phys. Rev. A* **52**, R2511 (1995).
- [61] Y. Chen and B. Zhang, *J. Phys. B* **45**, 215601 (2012).
- [62] A. Lohr, M. Kleber, R. Kopold, and W. Becker, *Phys. Rev. A* **55**, R4003 (1997).
- [63] R. de Nalda, E. Heesel, M. Lein, N. Hay, R. Velotta, E. Springate, M. Castillejo, and J. P. Marangos, *Phys. Rev. A* **69**, 031804(R) (2004).
- [64] Y. J. Chen, L. B. Fu, and J. Liu, *Phys. Rev. Lett.* **111**, 073902 (2013).